

PAPER • OPEN ACCESS

Estimating the NEMA characteristics of the J-PET tomograph using the GATE package

To cite this article: P Kowalski *et al* 2018 *Phys. Med. Biol.* **63** 165008

View the [article online](#) for updates and enhancements.

Related content

- [Time resolution of the plastic scintillator strips with matrix photomultiplier readout for J-PET tomograph](#)
P Moskal, O Rundel, D Alfs et al.
- [Simulations of a micro-PET system based on liquid xenon](#)
A Miceli, J Glistler, A Andreyev et al.
- [Calculation of the time resolution of the J-PET tomograph using kernel density estimation](#)
L Raczyski, W Wilicki, W Krzemie et al.

Programmable Motion for Image Acquisition, Treatment Planning & Dose Delivery



DYNAMIC THORAX PHANTOM MODEL 008A

The CIRS Dynamic Thorax Phantom is a precision instrument for investigating and minimizing the impact of tumor motion inside the lung. Ten interchangeable inserts are available for QA and dosimetry.

Viewray Dynamic Phantom
MODEL 008V



MIRIDIAN 



MRI-LINAC Dynamic Phantom
MODEL 008M

Dynamic Cardiac Phantom
MODEL 008C



CIRS
WWW.CIRSINC.COM

OPEN ACCESS

PAPER



Estimating the NEMA characteristics of the J-PET tomograph using the GATE package

RECEIVED
13 April 2018REVISED
25 June 2018ACCEPTED FOR PUBLICATION
11 July 2018PUBLISHED
10 August 2018

Original content from this work may be used under the terms of the [Creative Commons Attribution 3.0 licence](https://creativecommons.org/licenses/by/3.0/).

Any further distribution of this work must maintain attribution to the author(s) and the title of the work, journal citation and DOI.



P Kowalski¹, W Wiślicki¹, R Y Shopa¹, L Raczyński¹, K Klimaszewski¹, C Curcenu³, E Czerwiński², K Dulski², A Gajos², M Gorgol⁴, N Gupta-Sharma², B Hiesmayr⁵, B Jasińska⁴, Ł Kapłon², D Kisielewska-Kamińska², G Korcyl², T Kozik², W Krzemień⁶, E Kubicz², M Mohammed^{2,7}, S Niedźwiecki², M Pałka², M Pawlik-Niedźwiecka², J Raj², K Rakoczy², Z Rudy², S Sharma², S Shivani², M Silarski², M Skurzok², B Zgardzińska⁴, M Zieliński² and P Moskal²

¹ Department of Complex Systems, National Centre for Nuclear Research, 05-400 Otwock-Świerk, Poland

² Faculty of Physics, Astronomy and Applied Computer Science, Jagiellonian University, 30-348 Kraków, Poland

³ INFN, Laboratori Nazionali di Frascati, 00044 Frascati, Italy

⁴ Institute of Physics, Maria Curie-Skłodowska University, 20-031 Lublin, Poland

⁵ Faculty of Physics, University of Vienna, 1090 Vienna, Austria

⁶ High Energy Physics Division, National Centre for Nuclear Research, 05-400 Otwock-Świerk, Poland

⁷ Department of Physics, College of Education for Pure Sciences, University of Mosul, Mosul, Iraq

E-mail: pawel.kowalski@ncbj.gov.pl

Keywords: NEMA norms, J-PET, positron emission tomography, plastic scintillators

Abstract

A novel whole-body positron emission tomography (PET) system based on plastic scintillators is developed by the J-PET Collaboration. It consists of plastic scintillator strips arranged axially in the form of a cylinder, allowing the cost-effective construction of the total-body PET system. In order to determine the properties of the scanner prototype and optimize its geometry, advanced computer simulations were performed using the GATE (Geant4 application for tomographic emission) software.

The spatial resolution, sensitivity, scatter fraction and noise equivalent count rate were estimated according to the National Electrical Manufacturers Association norm, as a function of the length of the tomograph, the number of detection layers, the diameter of the tomographic chamber and for various types of applied readout. For the single-layer geometry with a diameter of 85 cm, a strip length of 100 cm, a cross-section of 4 mm × 20 mm and silicon photomultipliers with an additional layer of wavelength shifter as the readout, the spatial resolution (full width at half maximum) in the centre of the scanner is equal to 3 mm (radial, tangential) and 6 mm (axial). For the analogous double-layer geometry with the same readout, diameter and scintillator length, with a strip cross-section of 7 mm × 20 mm, a noise equivalent count rate peak of 300 kcps was reached at 40 kBq cc⁻¹ activity concentration, the scatter fraction is estimated to be about 35% and the sensitivity at the centre amounts to 14.9 cps kBq⁻¹. Sensitivity profiles were also determined.

1. Introduction

The National Electrical Manufacturers Association (NEMA), the association of electrical equipment and medical imaging manufacturers in the United States, publishes standards for medical diagnostic imaging equipment. One of its standards is NEMA-NU-2 (NEMA 2012), which pertains to positron emission tomography (PET) devices. It comprehensively defines the characteristics of PET scanners: the spatial resolution, scatter fraction, noise equivalent count rate (NECR) (Yang and Peng 2015), count losses and sensitivity. They allow us to compare different PET tomographs.

The subject of this article is the NEMA characteristics of a PET scanner with a large axial field of view (AFOV) and the dependence of these characteristics on the geometry of such a scanner. Examples of scanners with a large AFOV are: a 3D PET scanner based on lead-walled straw detectors (Lacy *et al* 2010), an RPC-PET based on resistive plate chambers (Crespo *et al* 2013), the first generation of the presently-developed total-body EXPLORER

PET (Cherry *et al* 2017, 2018, Viswanath *et al* 2017, Zhang *et al* 2017) and the Jagiellonian PET (J-PET) scanner based on the plastic scintillator strips (Niedźwiecki *et al* 2017). In this article we present the simulated NEMA characteristics of the J-PET.

The J-PET detector is a novel PET scanner built from axially arranged plastic scintillator strips (Moskal *et al* 2011, 2014, Moskal *et al* 2015, 2016), in contrast to the classical PET scanners which are based on inorganic crystal scintillators (Moses and Derenzo 1999, Moses 2003, Humm *et al* 2003, Townsend 2004, Karp *et al* 2008, Conti 2009, 2011, Slomka *et al* 2016). In the case of crystal tomographs, annihilation photons are registered using the photoelectric effect, while in the J-PET Compton scattering is used. In the J-PET, the relatively low detection efficiency (in comparison to crystal PET scanners) is compensated with the high time resolution of plastic scintillators, the application of few concentric detection layers, and the large AFOV of the detector (Moskal *et al* 2016). The use of plastic detectors opens allows the cost-effective construction of the total-body PET scanner. In such a total-body PET scanner, it would be possible to image a whole patient's body without moving the patient along the axis of the device. The total-body technique would increase the effective sensitivity, decrease the examination time and reduce the necessary image blur due to the patient's or scanner's movements when the whole body has to be examined. The clinical advantages of the total-body scanner are extensively discussed in Cherry *et al* (2017, 2018), Viswanath *et al* (2017) and Zhang *et al* (2017). For completeness, we emphasize here the possibility of a significant reduction in radiation dose needed for the whole-body scan, the possibility of using shorter lived tracers and the possibility of studying the kinetics in many organs simultaneously. Additionally, the dynamic range of total-body PET scanners is much broader than that of classical tomographs. This results in the fact that the radiotracers may be followed for a longer time before the signal decays to such an extent that it is not detectable. Also, the viability of multitracer studies is improved. Building a total-body PET scanner based on crystal scintillators is expensive⁸.

The much lower costs of building the J-PET scanner based on plastic scintillators (due to the less expensive detector material and reduced number of electronic channels) can make total-body PET diagnostics more widely available. In addition, in the J-PET solution with axially arranged plastic strips, the readout is placed outside the detection chamber, simplifying PET/MR hybrid construction and enabling the extension of the AFOV without a significant increase in costs. Moreover, the J-PET solution enables a detector to be built from multi-strip modules, the number of which can be adapted to the size of the patient. Such a modular J-PET can contribute to broader applications of cancer diagnostics, especially for larger patients and claustrophobic patients. A first prototype of such a portable and modular J-PET, with a 50 cm AFOV, is in the final stage of construction at the Jagiellonian University. This prototype consists of 24 modules, each with a weight of about 2 kg only (Moskal 2018).

The aim of this article is to present the NEMA characteristics of the J-PET scanner as a function of the length of the tomograph, the number of detection layers, the diameter of the tomographic chamber and the type of readout. The above characteristics may be used as a figure of merit in the geometry optimization of the prototype device. Because of the fact that the J-PET scanner is meant to be used in medical diagnostics, the target performance should be at least comparable to the performance of currently available commercial PET devices. In section 2 the principle of operation of the J-PET scanner is described. Section 3 defines the parameters of the tomograph considered in this article (section 3.1), a description of the data selection method, which was used to minimize the background from the annihilation photon scattered in the examined object or in the detector (section 3.2) and details about calculated characteristics sections 3.3–3.6. The final sections provide the obtained results (section 4) and the summary (section 5).

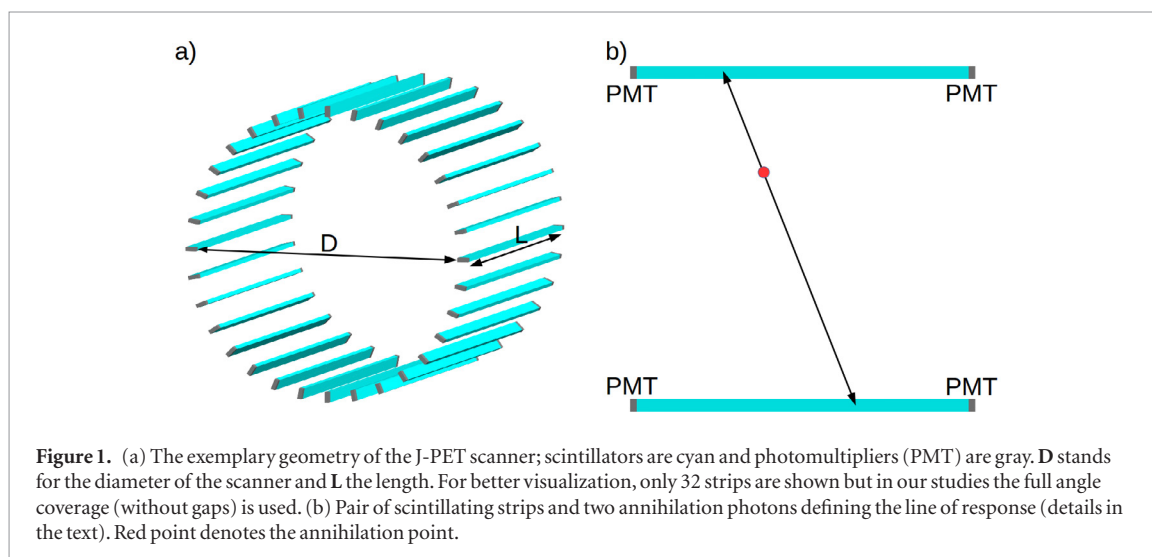
2. Principle of operation of the J-PET tomograph

The J-PET scanner is built from axially-arranged plastic scintillator strips. Each scintillator is read out by two photomultipliers located at the ends of the strip. Optical photons, generated in the scintillator due to the interaction of the gamma photon with the scintillator, propagate to the ends of the strip. Thus the scintillator strip acts also as a lightguide. In the photomultipliers, optical photons are converted into voltage signals and processed using dedicated front-end electronics boards (Pałka *et al* 2017) and the triggerless data acquisition system (Korcyl *et al* 2016, 2018). Data is stored locally and analyzed using the JPETFramework software (Krzemień *et al* 2015). Exemplary geometrical configuration of a single-layer J-PET tomograph is visualized in figure 1(a).

As in classical PET scanners, the J-PET detector registers back-to-back annihilation photons with an energy of 511 keV, outgoing from the investigated object. These photons come from annihilations of positrons emitted from the radionuclide (for example, ¹⁸F) with electrons in surrounding tissue.

The principle of operation of the J-PET may be explained using a simplified two-strip model (figure 1(b)). Knowing times of arrival of light signals to the ends of the strips, one can estimate the position of the interaction

⁸The first estimations of the commercial costs of such scanners points to about 10 million dollars (Cherry *et al* 2018).



of the 511 keV photon along the strip and the time of the scattering (Moskal *et al* 2014, 2015, Moskal *et al* 2016). In order to calculate these values, specialized algorithms were developed. In one of these algorithms, voltage signals at photomultipliers were reconstructed using the compressive sensing theory and, using these signals, times and positions of interactions were calculated (Raczyński L *et al* 2014, Raczyński *et al* 2015).

Experiments showed that an 80 ps hit-time resolution (standard deviation) for a 30 cm strip is achievable, allowing us to determine the position of the interaction along the strip with a spatial resolution of 2.2 cm (full width at half maximum (FWHM)). The fractional energy resolution for the energy deposited by the annihilation photon in the plastic scintillator strips was measured for a single strip J-PET prototype and it amounts to $\sigma(E)/E \approx 0.044/\sqrt{E(\text{MeV})}$ (Moskal *et al* 2014).

3. Materials and methods

The NEMA characteristics were estimated with the Geant4 application for tomographic emission (GATE) simulation toolkit (Jan *et al* 2004, 2011). The GATE software is based on the Geant4 framework (Agostinelli *et al* 2003), which is used to simulate interactions between radiation and matter. The GATE software was used to simulate a set of tomograph geometries with back-to-back two-gamma sources (defined by the points of electron-positron annihilations), corresponding to sources defined in the NEMA norm. Both primary and secondary scatterings of annihilation photons in the detector material were taken into account. Simulated times and positions of interactions were smeared using tomograph resolutions obtained experimentally. Further on, in order to reduce the fraction of events with gamma photons scattered in the phantom or in the detector, the signals were processed using selection criteria based on the correlations between the hit time, hit position and energy deposition of annihilation photons in the detector.

3.1. Main parameters of the simulated tomograph

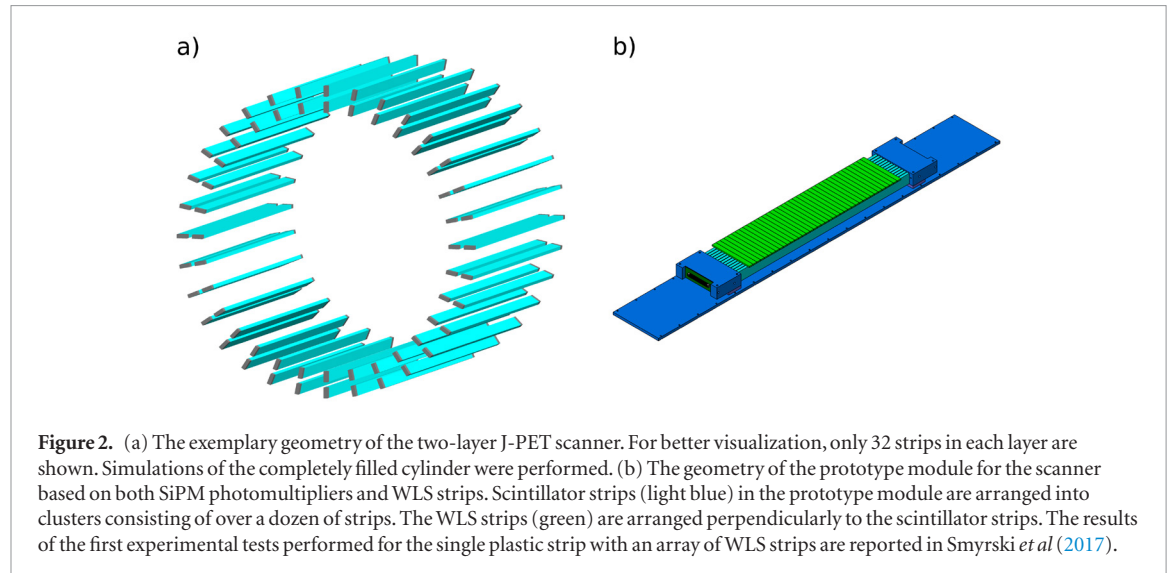
In this article we study the NEMA characteristics of the J-PET tomograph as a function of its length, diameter, number of detection layers, thickness of plastic strips and for three readouts: vacuum tube photomultipliers (PMT), silicon photomultipliers matrices (SiPM) and SiPMs combined with an additional wavelength shifters (WLS) layer (Smyrski *et al* 2017). Three diameters D of the detector chamber (75 cm, 85 cm and 95 cm), three lengths L (20 cm, 50 cm and 100 cm) and two thicknesses T (4 mm and 7 mm) of scintillators are taken into account, for both single- and double-layer geometries. The values of the diameter were chosen as typical for the presently available tomographs (Slomka *et al* 2016) and the axial field of view L will be tested in the range from the typical present tomographs (about 20 cm) to 100 cm. The diameter D (see figure 1) is defined as the distance between the inner walls of opposite strips. The number of strips depends on the diameter of the scanner and is calculated as the number of edges of the regular polygon circumscribed around the ring with the radius $D/2$ (see table 1).

For the two-layer geometries, the second layer consists of the same number of strips arranged in the cylinder with the radius 3 cm larger (figure 2(a)). The diameter of the double-layer geometry is defined as the distance between the inner walls of the opposite strips of the inner layer.

The depth (size of the strip along the radius of the scanner) of each scintillator is 20 mm and its thickness is 4 mm or 7 mm. Currently used crystalline tomographs have crystals with depths from 20 mm up to 30 mm,

Table 1. Number of strips in a single layer of the detecting chamber as a function of the thickness of the strip and the diameter of the chamber.

Thickness T (mm)	Diameter D (cm)		
	75	85	95
4	590	668	746
7	336	382	426



while their cross sections (perpendicular to the radius of the scanner) range from $4 \times 4 \text{ mm}^2$ to $6.3 \times 6.3 \text{ mm}^2$ (Slomka *et al* 2016, Vandenberghe *et al* 2016). The coincidence resolving time (CRT) and axial spatial resolution was simulated for three different readout solutions, referred to as the vacuum tube photomultipliers, silicon photomultipliers matrices or the SiPM readout with an additional layer of WLS strips (figure 2(b)). The WLS strips were arranged perpendicularly to the scintillator strips allowing for the determination of the gamma photon interaction point along the tomograph axis, based on the distribution of amplitudes of light signals in WLS strips (Smyski *et al* 2017). An analogical solution was proposed for the AX-PET detector (Casella *et al* 2014, Gillam *et al* 2014, Solevi *et al* 2015).

Configurations of all simulated cases are listed in table 2 and the used values of CRT and axial resolution as a function of the tomograph length L are shown in figure 3. The values of CRT and FWHM (in the z coordinate) for PMTs and SiPMs were estimated based on simulations presented in Moskal *et al* (2016) tuned to the empirical results for single- and double-strip J-PET prototypes (Moskal *et al* 2014, 2015). The FWHM with the additional layer of WLS strips was measured with the test setup described recently in the article (Smyski *et al* 2017). The values indicated as WLS-2 show the resolution achieved in the first test (Smyski *et al* 2017). However, since the system was not fully optimized, there is still room for significant improvement, which is indicated in figure 3 as WLS-1. The improvement may be achieved by better matching between the emission spectrum of the scintillator and the absorption spectrum of the WLS and a more efficient photon readout. In the test, only half of the WLS surface was covered by the SiPM.

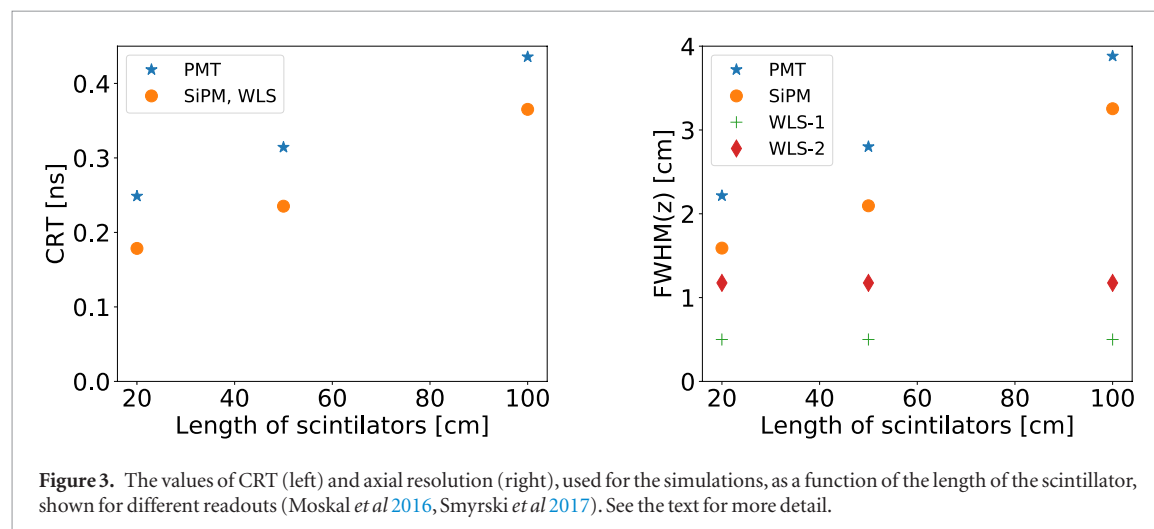
Simulations were performed using the list of physics processes called *emlivermore_polar* (Geant4 Collaboration 2016). This model is designed for any applications requiring a higher accuracy of electrons, hadrons and ion tracking without a magnetic field. Physical processes in the simulations include the photoelectric effect, Compton scattering, gamma conversion, Rayleigh scattering, ionisation and bremsstrahlung. Polarization of gamma photons is also simulated. The model describes the interactions of electrons and photons with matter down to 10 eV and up to 100 GeV, using interpolated data tables based on the Livermore library (Geant4 Collaboration 2016). This range of energies is well chosen for the purpose of the J-PET simulations due to the low energy cut on 10 keV. Energy thresholds and other selection criteria used in analysis are described in the following section.

3.2. Event selection method

An event is defined as a set of consecutive interactions of photons, originating from a single e^+e^- annihilation and all interactions of secondary particles. In the case of the J-PET detector, most of interactions are Compton scatterings. If the interactions are detected within the fixed time coincidence window of 3 ns, they are

Table 2. Configurations of simulated detecting systems which may differ with number of layers of the detector and their diameters, thickness, length of the scintillator strip and type of readout.

Layers	Thickness	L (cm)	D (cm)	Readout
1	4 mm	20	75	PMT
2	7 mm	50	85	SiPM
		100	95	SiPM + WLS



operationally considered to originate from the same annihilation event. Any two scatterings within an event may form a coincidence. Coincidences may be classified into three types: true, scattered and accidental.

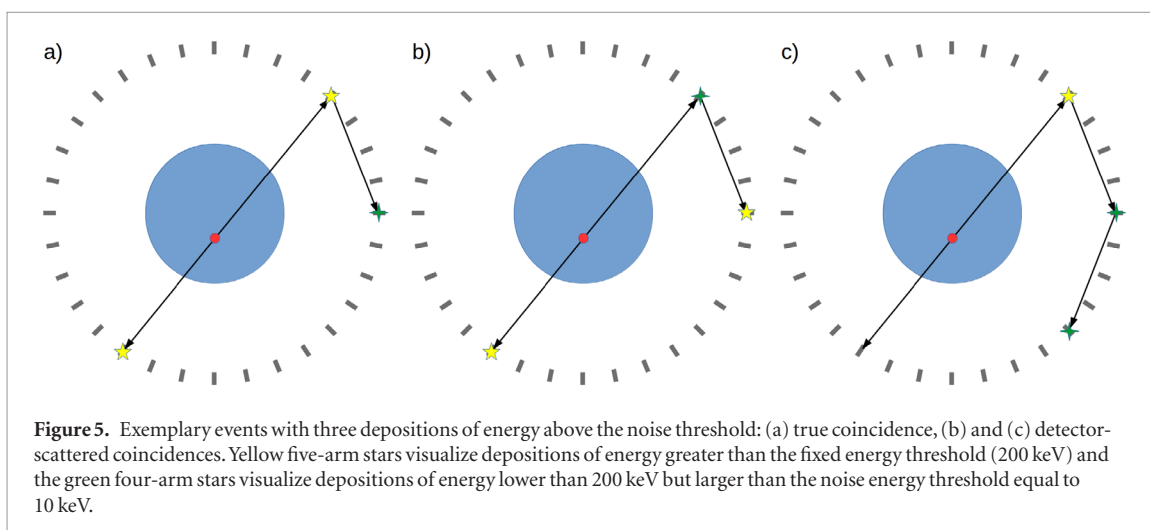
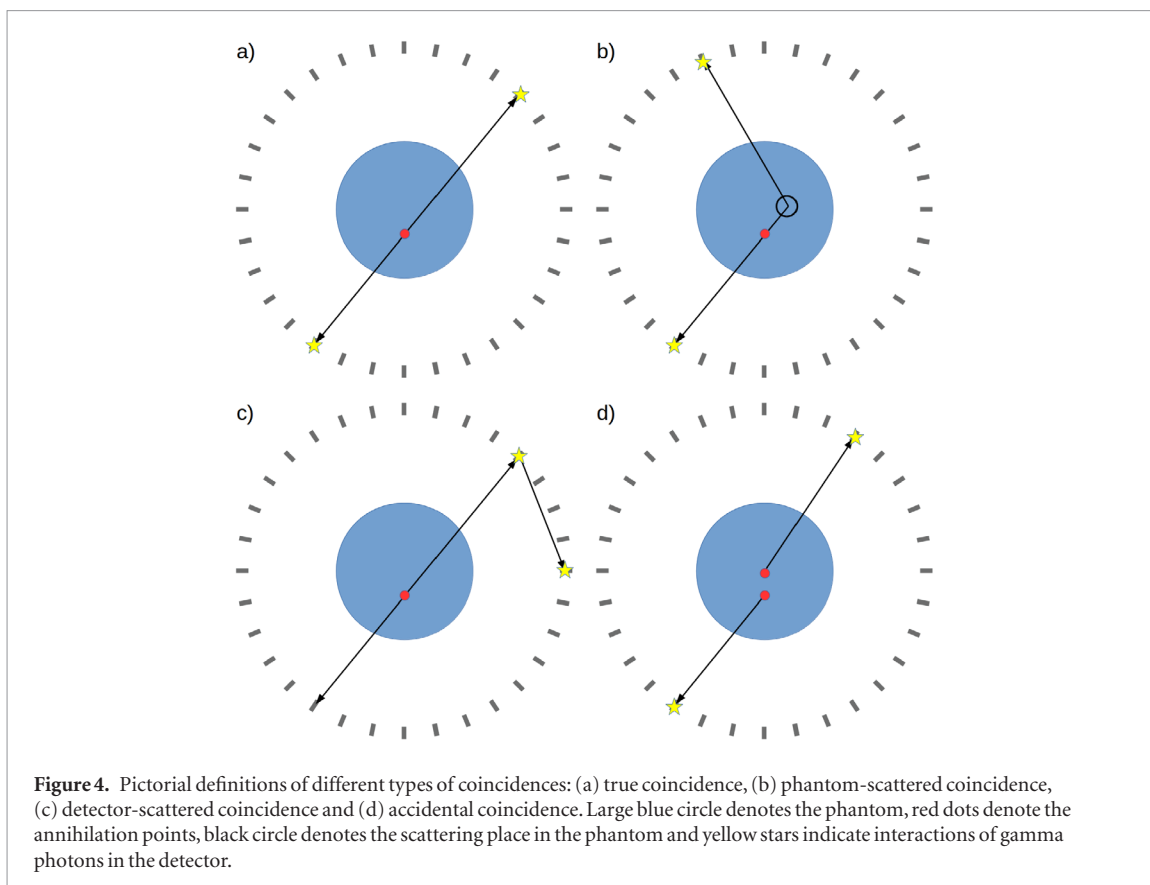
While true coincidences are desirable, the scattered and accidental coincidences contribute to the background, hinder the reconstruction of the image and decrease its final quality. Scattered coincidences may be divided into detector- and phantom-scattered coincidences. Detector-scattered coincidences are defined as coincidences in which at least one of the interactions does not originate from the annihilation photon but from another (often primary) scattering in the detector. Phantom-scattered coincidences are those in which at least one of the annihilation photons was scattered in the phantom before the detection. Coincidences of scatterings of photons from different annihilations are called accidental or random. Pictorial definitions of these different types of coincidences are shown in figure 4.

In order to extract true coincidences from the set of all coincidences, a two-level selection procedure is performed. In the first step, only events with exactly two interactions registered with an energy loss larger than 200 keV each, and any number of interactions with an energy loss larger than 10 keV (above the noise level) and smaller than 200 keV are accepted. We accept events with more than two scatterings in order to avoid rejection of such events as shown in figure 5(a), which can be classified as true coincidences. However, these conditions lead to the acceptance of unwanted coincidences shown e.g. in figures 5(b) and (c). Yet the requirement of at least two interactions with an energy loss above the 200 keV threshold reduces to a negligible level coincidences of the type shown in figure 5(c). This is because the 511 keV gamma photon cannot deposit more than 184 keV in more than one scattering (Kowalski *et al* 2016).

At the second level of the event selection, information about times and azimuthal angles⁹ of the scintillator strips is used. Time and azimuthal angle differences are calculated for each pair of hits. Using calculated values, parts of events are rejected. The selection criterion is based on the simulation with the cylindrical phantom (NEMA scatter phantom) and the linear source placed at the radial distance of 25 cm from the axis of the scanner (Kowalski *et al* 2016). The source was a 70 cm long rod with a diameter of 3.2 mm and activity of 1 MBq. The simulated geometry consisted of a single scintillator layer with strips that were 50 cm long and 7 mm thick and with a diameter of 85 cm. The simulation showed that all true coincidences lie in a well-defined region in the space spanned by the times and azimuthal angles differences. This region, which lies above the red line¹⁰ in figure 6, may be defined as a selection criterion. The longitudinal structure visible for a time difference near to 1.5 ns is caused by the phantom-scattered coincidences and it was discussed in Kowalski *et al* (2015).

⁹The azimuthal angle is the central angle in the plane perpendicular to the axis of the scanner. In figure 6 the azimuthal angle of scintillator A would be ACE.

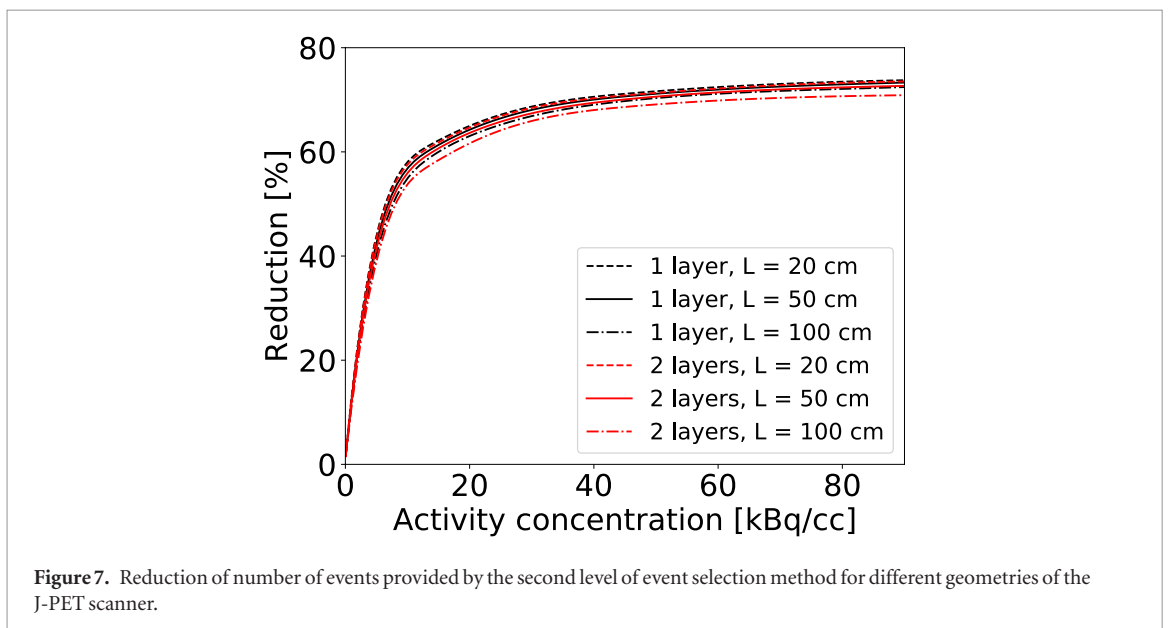
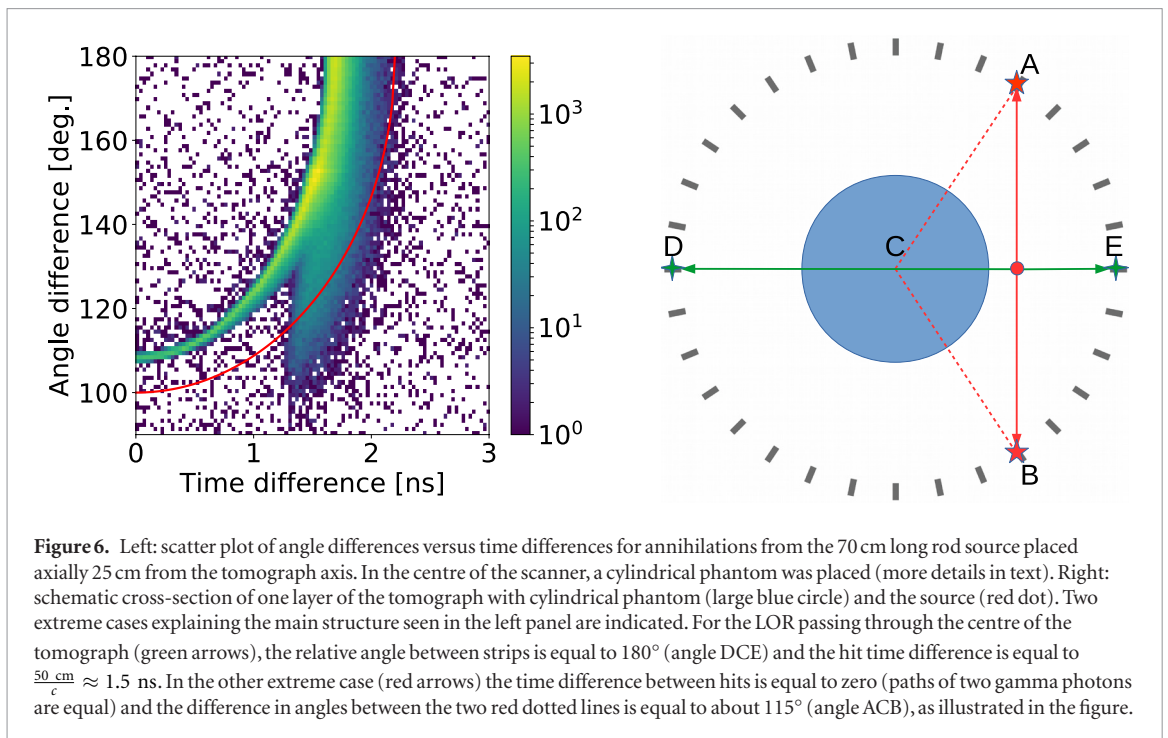
¹⁰The red line is the ellipse with a vertex at (2.2 ns, 180°), co-vertex at (0 ns, 80°) and center at (0 ns, 180°). The choice is based on results of simulations shown in figure 6. The choice of the red-line criterion is rather conservative and leaves room for further reduction of scatter fraction in the case of smaller objects imaging.



The selection criteria discussed above allow us to filter out most of the scattered coincidences from the true coincidences. The method is based on the values of deposited energies and times and azimuthal angle differences. The number of reduced events in the second level selection depends on the simulation type and the source activity. For the simulation with rod source placed at 25 cm from the axis of the scanner (figure 6), the percentage of rejected events (reduction factor with respect to the first level of selection) was 2.3%. In the case of spatial resolution simulations (section 4.2), the reduction was 0.5%. For the NECR simulations (section 4.3), the reduction was between 0.5% for small activity concentrations and about 70% for highest activity concentrations (about 90 kBq/cc), which shows that the higher the activity, the more important the reduction provided by the second level of event selection method (figures 7 and 8). The chosen selection criterion may also be adjusted to the size of the investigated object and to the geometrical properties of the scanner.

3.3. Sensitivity

The sensitivity of a positron emission tomograph is expressed as the true coincidence events rate, T normalized to the total activity A of the source. The selection criteria for the true coincidence were described in section 3.2. In particular, we require that each annihilation photon deposits at least 200 keV. This criterion limits registration



of photons scattered in the patient to the range from 0 to 60 degrees (Moskal *et al* 2016). In order to calculate the sensitivity, a linear 1 MBq source of back-to-back gamma photons with a length of 70 cm was simulated along the axis of the scanner in the centre of the AFOV. The NEMA norm requires that the activity should be such that the number of accidental coincidences is smaller than 5% of all prompt coincidences. The activity of 1 MBq fulfils that condition for all simulated geometries. The ratio of accidental coincidences ranges from 0.80% to 1.34%, depending on the geometry.

3.4. Spatial resolution

The spatial resolution of a PET scanner represents its ability to distinguish between two points after image reconstruction (NEMA 2012). In order to obtain this characteristic, signal determination from the annihilation must be performed and corresponding images must be reconstructed. The FWHM of the obtained distributions is referred to as point spread function (PSF) and is used as a measure of the spatial resolution.

Since the spatial resolution depends on the position inside the AFOV of the scanner, the PSF must be determined for six different, defined by the norm, positions. In the axial direction, the source should be placed at the

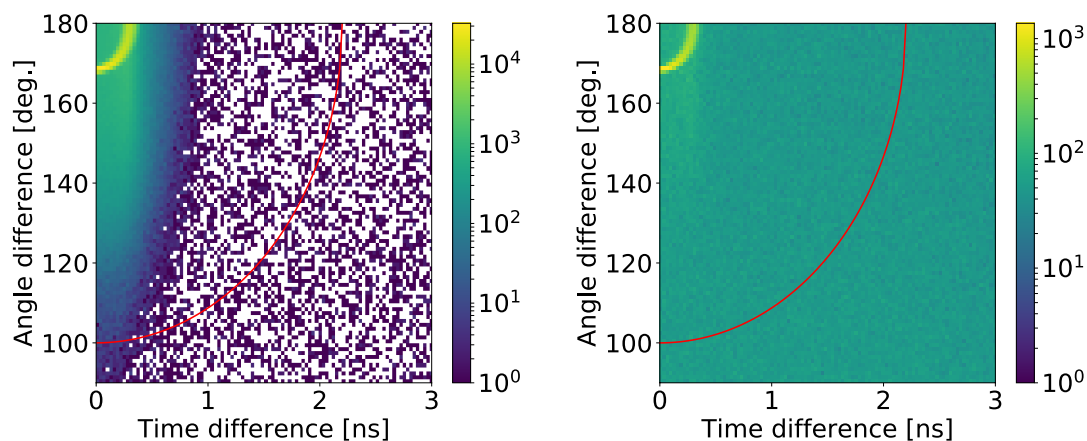


Figure 8. Results of the NECR characteristic simulation for the geometry with 50 cm long scintillating strips visualized in the form of scatter plots of angle differences versus time differences. The source was the 70 cm long rod placed axially inside the scatter phantom at a distance of 4.5 cm from the axis of the tomograph. The left panel shows the result of simulation for the small activity of 45 Bq cc^{-1} and the right panel for the high activity of 90.9 kBq cc^{-1} . The second level selection criterion indicated by the red line causes reduction of events by a factor of 0.5%–70% for the left and right panel, respectively.

centre of the AFOV and at the distance of three-eighths of the length of the AFOV from the centre of the scanner. In the transverse (i.e. radial) direction, the source should be placed at distances: 1 cm, 10 cm and 20 cm.

In the simulations, we used a back-to-back gamma source with a diameter of 1 mm. The activity of the source was sufficiently low (equal to 370 kBq [$10 \mu\text{Ci}$]) in order to fulfil the condition that the number of accidental coincidences should be less than 5% of all collected events. The ratio of the accidental coincidences for each simulated geometry and source position was smaller than 0.2%. According to the NEMA norm, the number of collected prompt coincidences for each position of the source should be at least 100 000.

After collecting the required number of events, a set of coincidence events was selected using the method described in section 3.2. Before reconstruction, the simulated data were smeared, taking into account experimental time and position resolution. After the selection and data smearing, reconstruction was performed. The smearing of position and time was performed for three different readout cases, as is shown in figure 3. For the reconstruction, according to the NEMA norm, the filtered back-projection (FBP) method was used. The 3D FBP algorithm from the software for tomographic image reconstruction (Thielemans *et al* 2012) package was used (Shopa *et al* 2017).

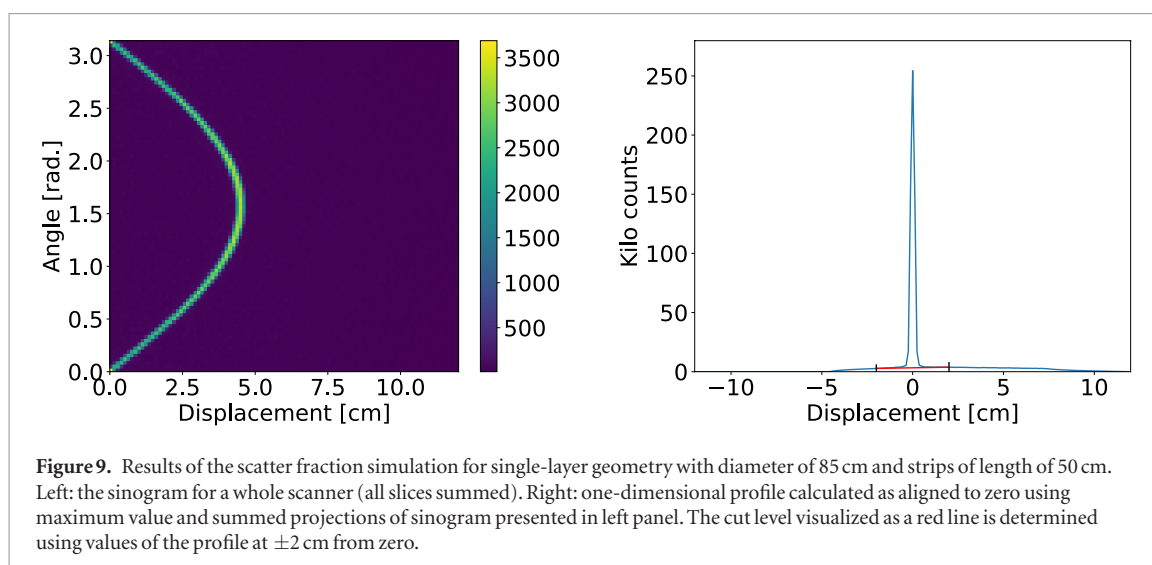
For each 3D image, a voxel with the maximum intensity was found and three one-dimensional profiles going through this voxel in each directions (x, y, z) were determined. For each profile, the values of FWHM were obtained. These values are interpreted as the spatial resolution of the scanner. Because of the variety of possible configurations of the J-PET scanner (taking into account parameters listed in section 3.1) only exemplary results for the single-layer geometries are presented in the article. Since the additional layer of strips influences mainly the detection efficiency, similar results should be expected for the double-layer geometries.

3.5. Scatter fraction

The scatter fraction of the PET scanner quantifies the sensitivity of the detector to scattered radiation. It may be simply expressed as a ratio between the scattered coincidences and the sum of the scattered and the true coincidences. In the case of the J-PET detector, built from plastic scintillators, the annihilation photon interacts via Compton scattering and there is a significant fraction of events (depending on the detector geometry) when the annihilation photon undergoes more than one scattering in the detector. Therefore, in the case of the J-PET tomograph, the scattered coincidences consist of the detector- and phantom-scattered coincidences. However, applying the fixed energy threshold (200 keV) means that most of the detector-scattered coincidences are reduced (see section 3.2 and Kowalski *et al* (2016) for more details).

The simulated phantom is a solid cylinder made of polyethylene with an outside diameter equal to 203 mm and a length of 700 mm. Parallel to the axis of the cylinder, a hole of diameter 6.4 mm is drilled in a radial distance from the axis of the phantom equal to 45 mm. A line source insert is also made of polyethylene and it is a tube with the inside diameter 3.2 mm and the outside diameter of 4.8 mm. The tube may represent known activity and be placed inside the hole of the phantom.

In the simulation used to obtain the scatter fraction of the J-PET scanner, the source of back-to-back annihilation photons with an activity of 1 kBq was generated. The value of the activity for obtaining the scatter fraction is limited by the condition that the ratio between the random and true coincidences should be smaller than 1% (NEMA 2012). For such a small activity, there were only single accidental coincidences per each data set consist-



ing of hundreds of thousands of prompt coincidences, which means that the activity of 1 kBq fulfils this condition. The NEMA norm also requires that the number of acquired prompt coincidences must be at least 500 000. In our studies, the number of prompt coincidences was one million.

As a first step of the data processing, the space inside the scanner is axially divided into N virtual slices and N^2 oblique sinograms are generated. The sinogram is a transformation of the line of response (LOR) into a pair of values: the distance of this LOR to the centre of the detector (in the x - y plane) and the angle between the LOR and the x axis of the cross section of the scanner. In the second stage, oblique sinograms are converted into rebinned sinograms using the single slice rebinning algorithm. The number of rebinned sinograms is equal to $2N-1$. After that, rebinned sinograms are merged into one sinogram (example in the left panel of figure 9). Using this summed sinogram, all projections are aligned with maximum value to zero and summed in order to get a one-dimensional profile (an example of such a profile is shown in the right panel of figure 9). After summing up, the values of such obtained profiles at distances ± 2 cm from zero are calculated. The area of the profile over the line crossing two points at ± 2 cm is treated as true coincidences, whereas the area below this line corresponds to the scattered (and accidental) coincidences.

The scatter fraction was calculated for six geometries: one or two scintillator layers and three lengths L of scintillators: 20 cm, 50 cm and 100 cm. The diameter of the detector chamber was 85 cm and the profile of the single scintillator was 20 mm \times 7 mm.

3.6. Noise equivalent count rate

The NECR is a characteristic that shows the effect of a correction for scattered and random coincidences as a function of the source activity, and it is a measure of the effective sensitivity of the scanner (Conti 2009). The NECR may be defined as: $NECR = \frac{T^2}{T+S+R}$, where T stands for the rate of true coincidences, S —scattered coincidences, R —random (accidental) coincidences.

The NECR characteristic is a figure of merit showing the optimal value of activity of the source for a fixed geometry of the scanner. The optimal value is defined by the position of the NECR peak. The smaller the value of the activity at the peak, the smaller the activity that may be applied to the patient in order to get the best possible results. The NECR is also related to the image quality SNR (signal-to-noise ratio) (Yang and Peng 2015).

The method of obtaining the NECR is similar to the method of measuring and calculating the scatter fraction. While the scatter fraction is measured for single activity of the source, the NECR varies as a function of the activity.

4. Results

4.1. Sensitivity

The values of sensitivity for different geometries of the J-PET scanner are presented in figure 10. All events were grouped into slices in order to obtain sensitivity profiles. Grouping was done using information from the simulation about the exact position of the place of emission of annihilation photons for each coincidence.

Profiles of sensitivity are presented in figure 11. Since the length of the phantom was equal to 70 cm, the profiles are presented only for positions in the range -35 cm to 35 cm (along the axis of the scanner).

One can see that the values of sensitivities obtained for single- and double-layer geometries with the same diameters and lengths of strips, differ by about three times. At first, one could suppose that the sensitivity for

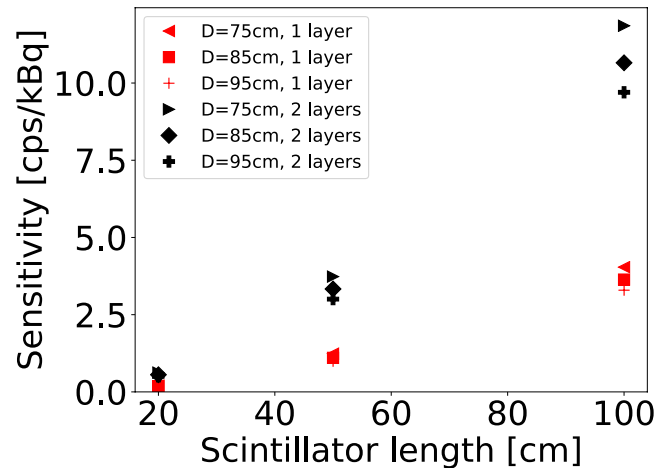


Figure 10. General sensitivities for different geometries of the J-PET scanner.

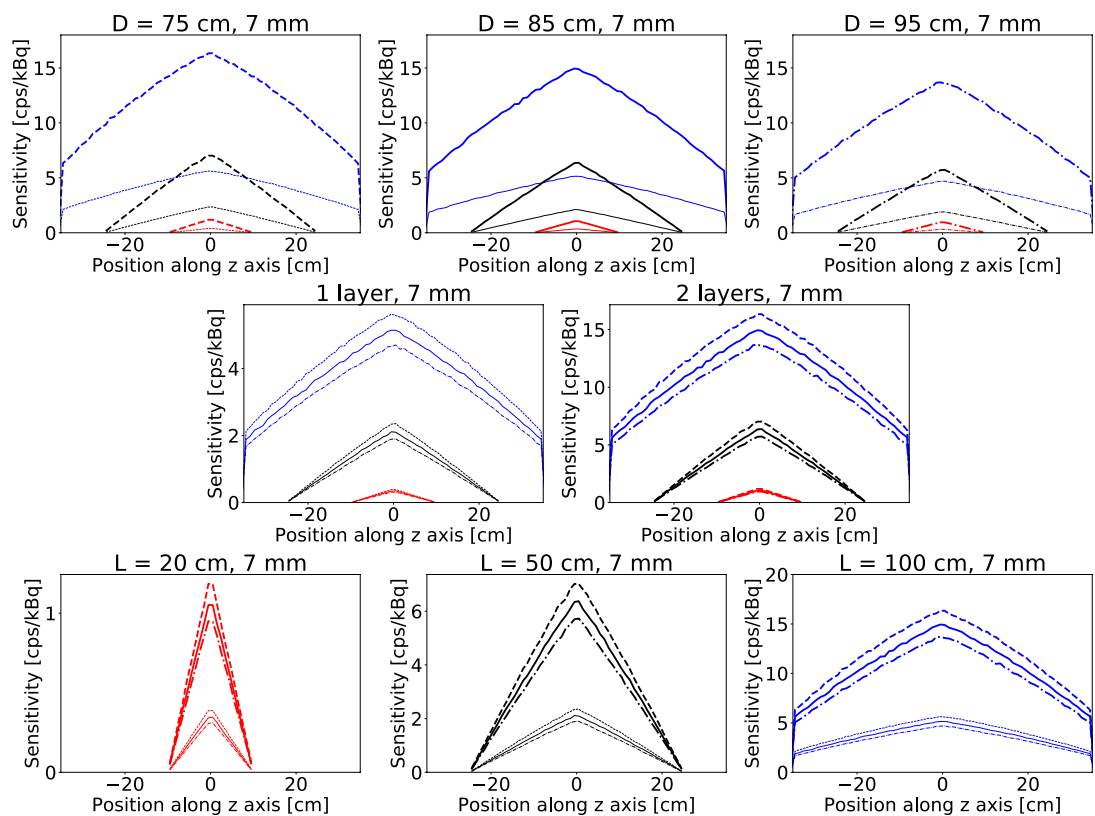


Figure 11. Sensitivity profiles grouped by the diameter of the detecting chamber (first row), number of layers (second row) and lengths of the scintillators (third row). Legend: $D = 75$ cm (dashed - -), $D = 85$ cm (solid -), $D = 95$ cm (dashed-dotted -.), one layer (thin lines), two layers (thick lines), $L = 20$ cm (red), $L = 50$ cm (black), $L = 100$ cm (blue).

the double-layer geometry would be almost four times bigger than for the corresponding single-layer geometry. However, there are two reasons that the ratio between the corresponding sensitivities is about three. Firstly, the probability of detection of the single gamma photon with two layers is about 1.82 times bigger than with one layer (the efficiency of the registration of the 511 keV photon in the first layer is equal to about 17.8%). This means that the probability of registration of the coincidence with double-layer geometry would be about $1.82^2 = 3.31$ times higher than for single-layer geometry with the same strip length. Secondly, not all true coincidences are properly registered due to the fact that if beside the scatterings forming the true coincidence, the additional (scattered or accidental) interaction occurs during the time window, the event is rejected. The effect becomes stronger as the detection efficiency increases (which grows with the number of layers and with the length of the strips). Both of these effects lead to the fact that the improvement factor, in terms of sensitivity, is only about three.

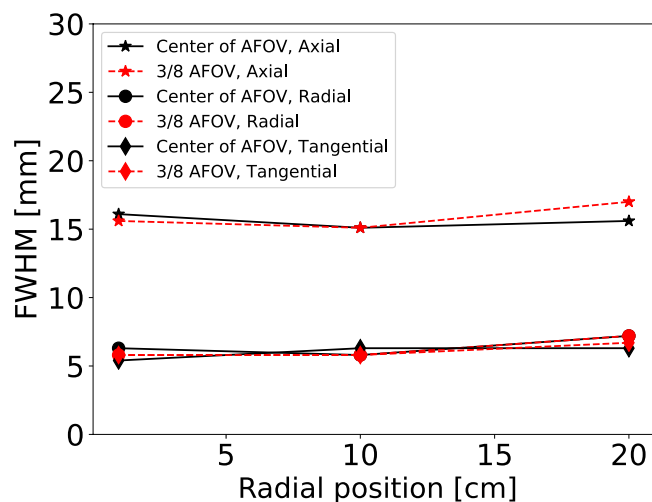


Figure 12. Spatial resolution in three directions—radial, tangential and axial. The geometry was fixed to the single layer chamber with the diameter of 85 cm and strips with a length of 50 cm and a thickness 7 mm. Hit-time and hit-position resolutions were used as anticipated for the SiPM readout.

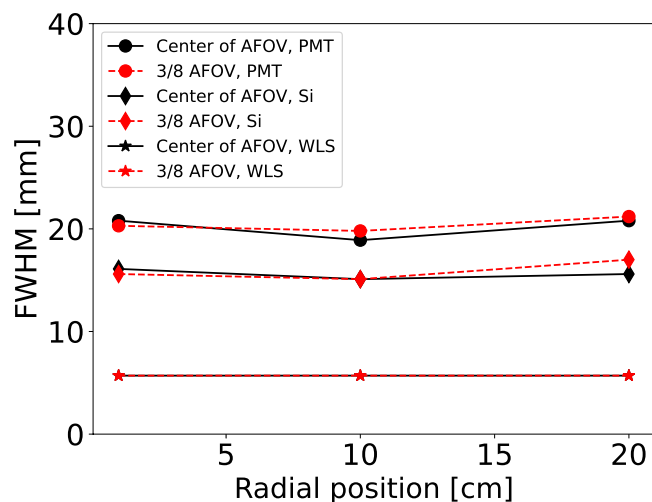


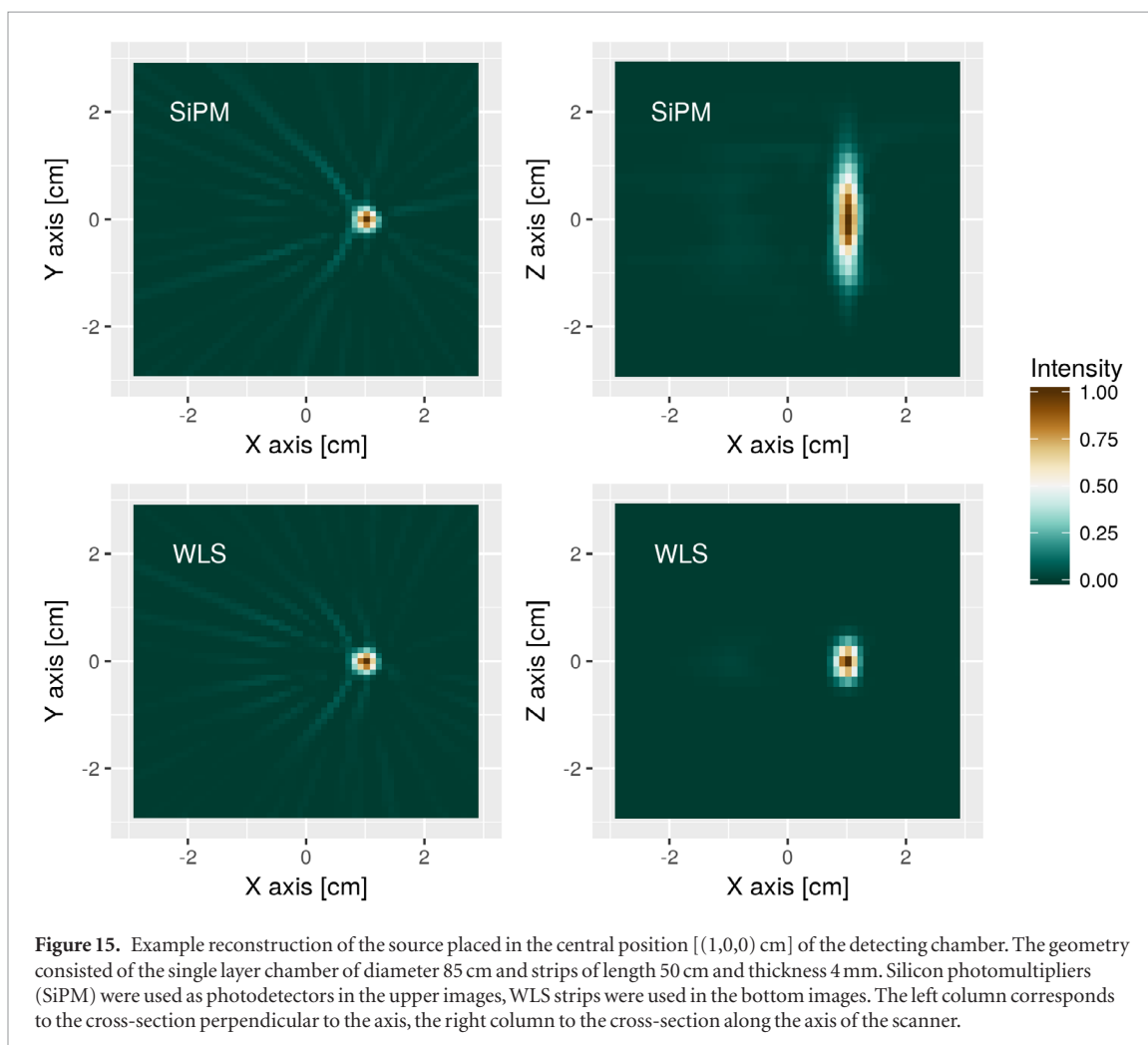
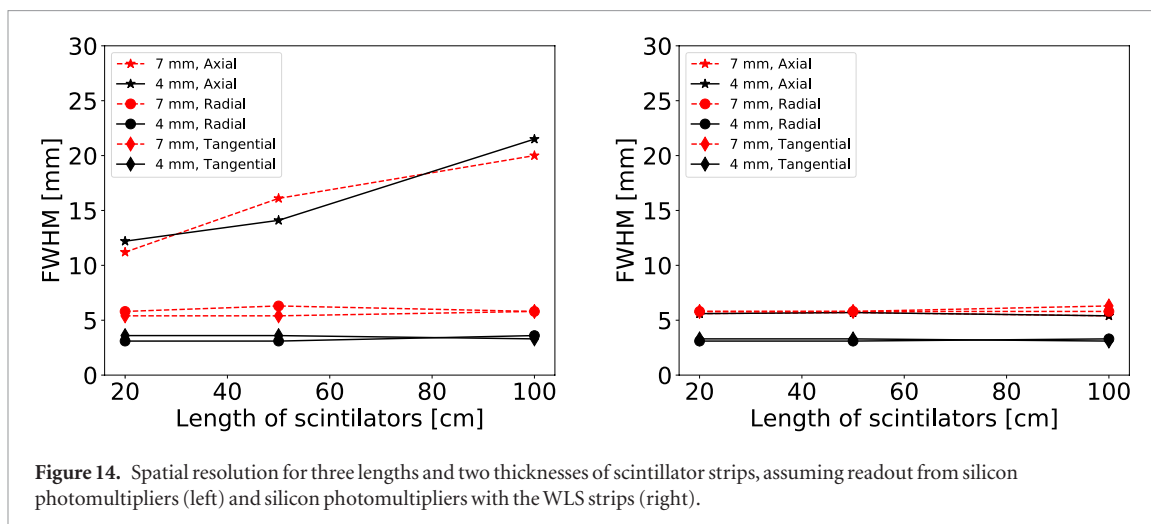
Figure 13. Axial resolution for different types of optical photon detectors attached to scintillator strips and two axial positions as a function of radial position of the source. Presented results were obtained for the single-layer geometry with a diameter of 85 cm and strips of length 50 cm and thickness 7 mm. Note that the results for WLS at the centre (black stars) and at 3/8 AFOV (red stars) overlap.

Adding the second layer of strips increases the detection efficiency. However, the rate of the detector-scattered and accidental events grows faster than the rate of true coincidences. This is because in the case of two layers there is additional probability of interlayer scatterings which are not increasing the rate of true coincidences but may increase the rate of scattered and accidental coincidences.

4.2. Spatial resolution

The results were selected in order to show the influence of each parameter on the final spatial resolution of the scanner. Firstly, the influence of the axial position of the scanner was investigated. The geometry was fixed to the single layer chamber with the diameter of 85 cm and strips with length of 50 cm and thickness equal to 7 mm. Hit-time and hit-position resolutions were used as anticipated for the SiPM readout. Results are presented in figure 12. All resolutions seem to be slightly dependent on the radial position of the source. There is also no visible difference between resolutions for sources placed in the centre of the AFOV and in 3/8 of the AFOV.

Secondly, the type of optical photon detector attached to the strip was taken into account (PMT, SiPM or WLS). The geometry was fixed to the single layer chamber with a diameter of 85 cm and strips of length 50 cm and thickness equal to 7 mm. Results for different types of detectors are presented in figure 13. It is important to note that only axial spatial resolution depends on the kind of anticipated light readout. Simulations confirmed intuition, viz. that the smaller the experimental uncertainty, the better the axial resolution. Additionally, they showed that if the number of collected coincidences is large enough, the spatial resolution barely depends on the position of the source along the axis of the scanner.



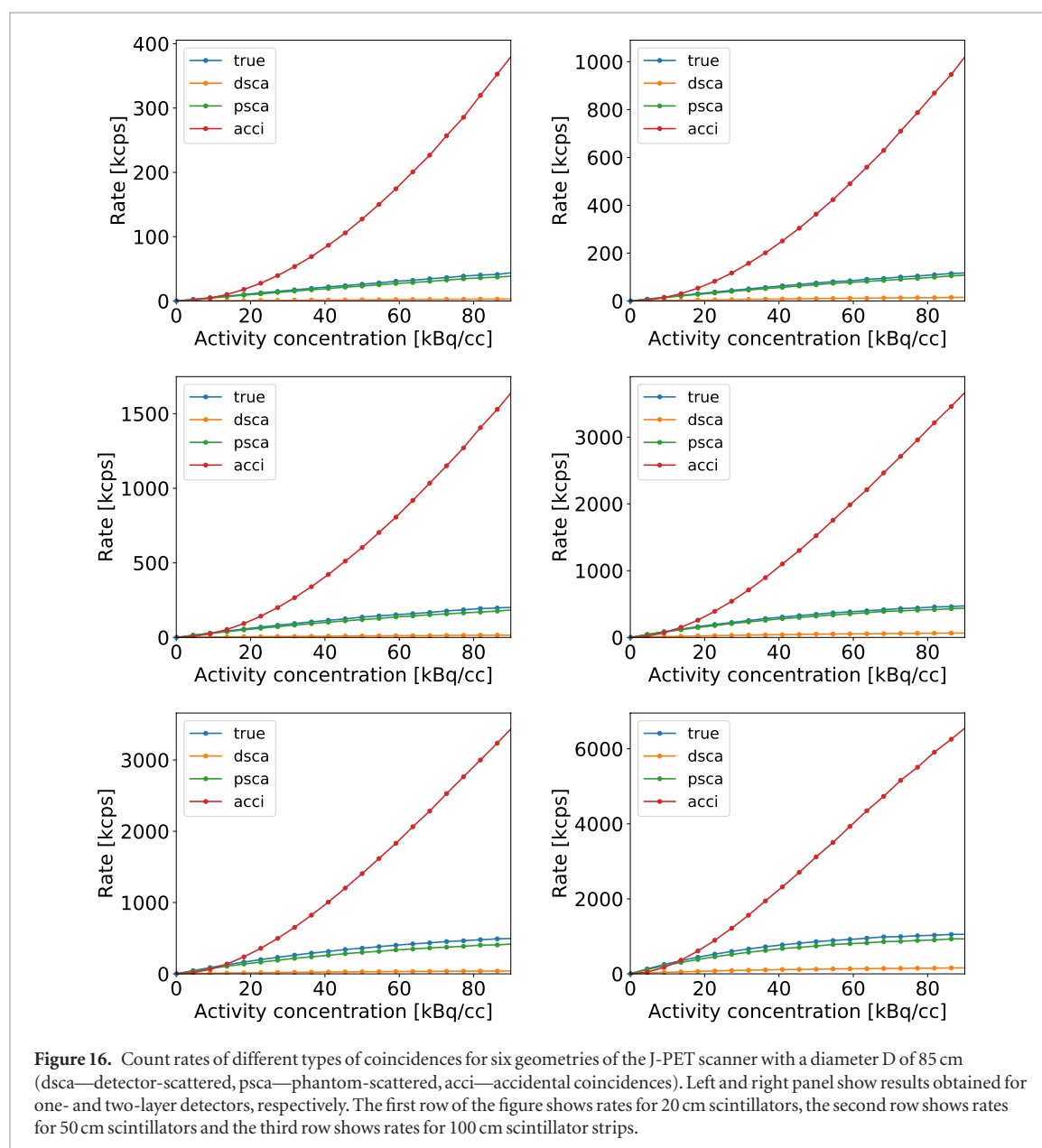
Finally, the geometry of the single strip was taken into account. Results for three lengths and two thicknesses of scintillator strips are presented in figure 14. The position of the source in each case was fixed to $(1, 0, 0)$ cm (only 1 cm from the centre of the tomograph). Simulations showed that, as expected in the case of the J-PET without WLS readout, the axial resolution worsens proportionally to the length of the strip (left panel of figure 14). However, it improves and remains constant along the scanner in the case of the readout with the WLS layer (right panel of figure 14). Because of the axial symmetry of the detecting chamber, radial and tangential resolutions are independent of the length of the strip. For each type of resolution, better results are obtained for thinner strips (4 mm), e.g. for the radial and tangential resolution, they are reduced twice with respect to results obtained with strips of 7 mm thickness. For the axial resolution there is a slight difference between geometries with 4 mm and 7 mm thick strips.

Table 3. Scatter fraction for six geometries of the J-PET scanner calculated using the method based on sinograms analysis.

Nr of layers	$L = 20$ cm (%)	$L = 50$ cm (%)	$L = 100$ cm (%)
1	36.0	35.8	34.8
2	35.1	35.6	34.7

Table 4. Scatter fraction for six geometries of the J-PET scanner calculated using the method based on true Monte Carlo.

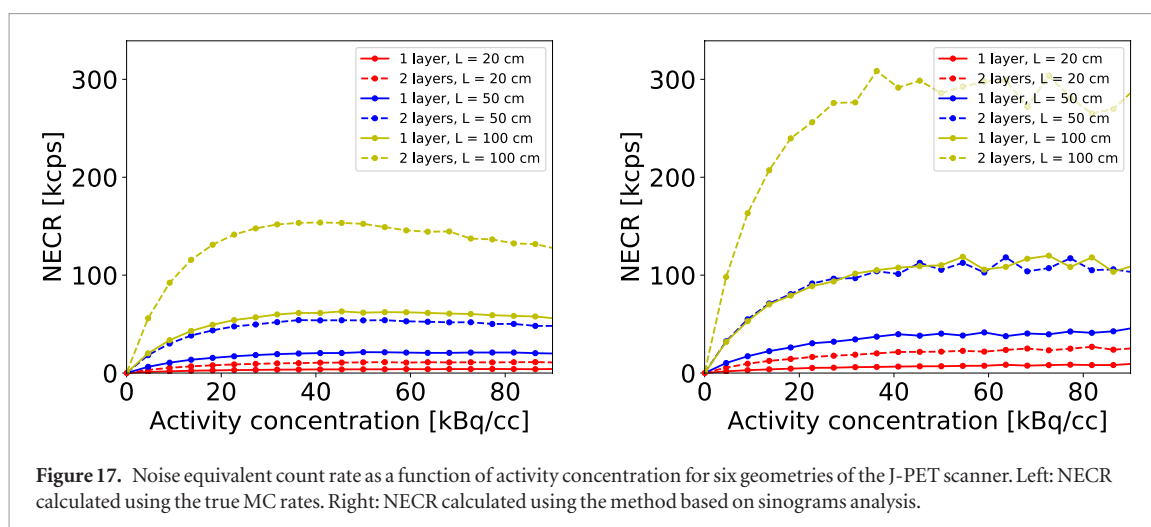
Nr of layers	$L = 20$ cm (%)	$L = 50$ cm (%)	$L = 100$ cm (%)
1	49.1	49.1	47.6
2	51.1	51.2	50.1

**Figure 16.** Count rates of different types of coincidences for six geometries of the J-PET scanner with a diameter D of 85 cm (dsca—detector-scattered, psca—phantom-scattered, acci—accidental coincidences). Left and right panel show results obtained for one- and two-layer detectors, respectively. The first row of the figure shows rates for 20 cm scintillators, the second row shows rates for 50 cm scintillators and the third row shows rates for 100 cm scintillator strips.

An example of the reconstruction of the source placed in the centre of the tomograph may be seen in figure 15 (geometry was fixed to the single layer chamber with a diameter of 85 cm and strips of length 50 cm and thickness equal to 4 mm; silicon photomultipliers were used as photodetectors).

4.3. Scatter fraction

Results obtained using the method based on the sinogram analysis are presented in table 3. The scatter fraction was also calculated using the true Monte Carlo information about types of coincidences in each event. Results for such calculations are presented in table 4. Values obtained for these six geometries are consistent with the



value calculated in previous studies for one layer 384 strip geometry (Kowalski *et al* 2016). The scatter fraction calculated from sinogram analysis is smaller than from the identification of events based on the information from Monte Carlo simulations. A similar effect was reported in Yang and Peng (2015).

4.4. Noise equivalent count rate

Firstly, rates of the true, scattered and accidental coincidences were calculated (figure 16). Simulations were performed for activity concentrations in the range 0 to about 90 kBq cc^{-1} (the activity of the source put inside the phantom was in the range of 1 MBq to 2000 MBq).

Secondly, the NECR characteristic was calculated (figure 17). As one can see, peaks for single layer tomographs are obtained for higher activity concentrations than for two layer scanners (for the same length of strips). On the other hand, the longer the strips, the lower the value of activity concentration, for which the peak is obtained. The best results were obtained for the geometry with two layers and 100 cm long strips. For this geometry, the NECR peak was about 300 kcps for activity concentration of about 40 kBq cc^{-1} , for the method based on the sinograms analysis. The method based on the true MC gives characteristics which are about two times lower than in the case of characteristics obtained using the sinograms analysis. This is due to a usage of a 12 cm radius cylindrical cut in the processing of sinograms (NEMA 2012, Yang and Peng 2015).

5. Summary

Studies presented in this article cover the estimation and the analysis of the NEMA norms for the J-PET scanner. Investigations were performed using the GATE software. The spatial resolution, the scatter fraction, the NECR and the sensitivity were estimated according to the NEMA norm as a function of the length of the tomograph, the number of detection layers, the diameter of the tomographic chamber and as a function of the applied type of readout.

Firstly, the sensitivity profiles were estimated for three lengths of scintillator strips (20 cm, 50 cm, 100 cm), three diameters of detecting chamber (75 cm, 85 cm, 95 cm) and two thicknesses of scintillators (4 mm, 7 mm). The sensitivity increases with the length of the scintillator and with the number of layers (it is greater for two-layer geometries than for one-layer geometries). On the other hand, the larger the diameter of the detecting chamber, the lower the sensitivity.

For a two-layer geometry with a diameter equal to 85 cm and with 50 cm scintillating strips, the sensitivity at the centre of the tomograph was about 6.3 cps kBq^{-1} while for 100 cm strips it exceeded $14.9 \text{ cps kBq}^{-1}$. The sensitivity of the double-layer J-PET with 100 cm AFOV is in the range of typical values of modern commercial PET scanners. For example, the sensitivity for the GE Discovery IQ, measured at the centre and at 10 cm, is 22.8 and $20.4 \text{ cps kBq}^{-1}$ (Reynés-Llompарт *et al* 2017), while for the Philips Vereos it is about 21 cps kBq^{-1} (Philips 2018a).

For each geometry configuration, the spatial resolution was calculated for six different positions of point source inside the detecting chamber. All resolutions seem to be independent of the radial distance of source from the axis of the scanner. While tangential and radial resolutions are independent of the length of the detecting strips, the axial resolution increases as the length of the strips decrease.

The spatial resolution is strongly dependent on the type of readout simulated. The shorter the CRT time and PSF(z), the better the resolution. While in the current J-PET prototype the vacuum tube photomultipliers are used, in the next prototypes they will be replaced with silicon photomultipliers and WLS strips in order to reach a higher class resolution.

Simulations showed that when silicon photomultipliers were used (for a geometry with a diameter of 85 cm, with strips of length 100 cm and thickness equal to 4 mm), the spatial resolution (PSF) in the centre of the scanner is about 3 mm (radial, tangential) and 20 mm (axial). If an additional layer of WLS were used to improve the readout, the axial resolution would be equal to 6 mm. This is comparable to values of spatial resolutions for currently used commercial PET scanners. For example, the GE Discovery IQ has a spatial resolution in the range of 4.2 mm at 1 cm to 8.5 mm at 20 cm (Reynés-Llompарт *et al* 2017). Similar resolutions (about 5 mm) are also obtained for Philips Gemini TF PET/CT (Surti *et al* 2007, Philips 2018b), Philips Vereos (4 mm) (Philips 2018a) and Siemens Biograph TM (Gonias *et al* 2007, Siemens 2018).

The scatter fraction was calculated for six geometries of the J-PET scanner with three different lengths of strips and one or two layers of scintillators. The cylindrical NEMA phantom was used for simulations. The values of scatter fraction are strongly dependent on the method used in order to calculate the characteristic. If the method based on sinogram analysis was used, the scatter fraction was in the range of 34.7% (two layers, 100 cm strips) to 36.0% (one layer, 20 cm strips). On the other hand, if the method based on the true Monte Carlo was used, the scatter fraction was in the range of 50.2% (two layers, 50 cm strips) to 47.6% (one layer, 100 cm strips).

Obtained values of scatter fraction are similar to those computed and measured for commercial PET scanners. For example, the GE Discovery has a scatter fraction of between 21% and 34%, dependent on the mode used (2D or 3D) (Teras *et al* 2007). The newest model of GE tomograph—Discovery IQ—has a scatter fraction of 36.2% (Reynés-Llompарт *et al* 2017).

The next characteristic from the NEMA norm is the NECR dependency. The NECR was obtained for geometries listed above for scatter fraction and for the same cylindrical phantom. The activity concentration ranges from 0 to about 90 kBq cc⁻¹ (figure 17). The simulations showed that the longer the strips, the higher the value of NECR peak, and it is obtained for a smaller value of activity concentration. The smaller the activity concentration, the smaller the dose deposited in the patient's body, and the shorter the recuperation.

The best results for NECR were obtained for two-layer geometry with 100 cm scintillator strips. The NECR peak for this geometry was equal to about 300 kcps and it was achieved at about 40 kBq cc⁻¹. For two-layer geometry with 50 cm strips the NECR peak of 110 kcps was reached at 63 kBq cc⁻¹.

For commercial PET scanners, the values of NECR peak are strongly dependent on the model of the tomograph. For example, the GE Discovery achieves a NECR peak of 84.9 kcps at 43.9 kBq cc⁻¹ (2D) and 67.6 kcps at 12.1 kBq cc⁻¹ (3D) (Teras *et al* 2007), the GE Discovery IG achieves a NECR peak of 124 kcps at 9.1 kBq cc⁻¹ (Reynés-Llompарт *et al* 2017) and the Siemens Biograph mCT achieves 186 kcps at 30.1 kBq cc⁻¹ (Karlberg *et al* 2016). This places the J-PET scanner in the range of typical values. However, current studies show that there is room for a significant improvement in the reduction of the random background, which leads to higher values of NECR peaks and finally to images of higher quality (Oliver and Rafecas 2016).

The best spatial resolutions were obtained for the 4 mm thick strips and the SiPM readout with an additional layer of WLS strips. Adding a second cylindrical layer of strips seems to have a slight influence on the spatial resolution and the scatter fraction, but it strongly improves the sensitivity and the NECR characteristics. Increasing the diameter of the detecting chamber worsens the sensitivity of the scanner. The longer the strips, the higher the sensitivity, the higher the NECR peak (which is obtained for smaller values of the activity concentration) and the smaller the scatter fraction. On the other hand, without WLS strips, the axial resolution worsens as strip length increases. In order to take into account all the above figures of merit in the process of projecting the J-PET prototype, a compromise must be found between the geometrical acceptance, the background, the image quality and the production cost. It seems that from all tested geometries, the best results were obtained for the double-layer geometry built from strips of length 100 cm and thickness 4 mm, the diameter equal to 75 cm, and the SiPM photomultipliers with the additional layer of WLS strips used as readout.

The above studies confirmed that the PET scanner based on plastic scintillator strips may achieve NEMA characteristics comparable to those obtained for commercially used PET scanners. We believe that the presented results may be improved. For example, the method of events selection (section 3.2) may be optimized. Preliminary studies showed that there is a strong dependence between the maximal number of additional hits in an event (with energies between 10 keV and 200 keV), the value of the noise energy threshold and the values of the presented characteristics. The design of the scanner may also be optimized by the shapes of the strips and the number of scintillator layers, and it will be improved in future prototypes.

Acknowledgments

We acknowledge the technical and administrative support of A Heczko, M Kajetanowicz, and W Migdał, and the financial support of The Polish National Center for Research and Development through grant INNOTECH-K1/IN1/64/159174/NCBR/12, the Foundation for Polish Science through MPD and TEAM/2017-4/39 programmes, the National Science Centre through grant Nos. 2016/21/B/ST2/01222, 2017/25/N/NZ1/00861, the Ministry for Science and Higher Education through grant Nos. 6673/IA/SP/2016, 7150/E-338/SPUB/2017/1, the EU and

MSHE grant No. POIG.02.03.00-161 00-013/09. BCH acknowledges support from the Austrian Science Fund (FWF-P26783).

References

- Agostinelli S et al 2003 Geant4—a simulation toolkit *Nucl. Instrum. Methods Phys. Res. A* **506** 250–303
- Casella C et al 2014 A high resolution TOF-PET concept with axial geometry and digital SiPM readout *Nucl. Instrum. Methods Phys. Res. A* **736** 161–8
- Cherry S R et al 2017 Total-body imaging: transforming the role of positron emission tomography *Sci. Trans. Med.* **9** 1–7
- Cherry S R et al 2018 Total-body PET: maximizing sensitivity to create new opportunities for clinical research and patient care *J. Nucl. Med.* **59** 3–12
- Conti M 2009 State of the art and challenges of time-of-flight PET *Phys. Med.* **25** 1–11
- Conti M 2011 Focus on time-of-flight PET: the benefits of improved time resolution *Eur. J. Nucl. Med. Mol. Imaging* **38** 1147–57
- Crespo P et al 2013 Resistive plate chambers in positron emission tomography *Eur. Phys. J. Plus* **128** 73
- Geant4 Collaboration 2016 Geant4—physics reference manual <http://geant4.web.cern.ch/geant4/UserDocumentation/UsersGuides/PhysicsReferenceManual/fo/PhysicsReferenceManual.pdf> (Accessed: 29 March 2018)
- Gillam J E et al 2014 Sensitivity recovery for the AX-PET prototype using inter-crystal scattering events *Phys. Med. Biol.* **59** 4065–83
- Gonias P et al 2007 Validation of a GATE model for the simulation of the Siemens biographTM 6 PET scanner *Nucl. Instrum. Methods Phys. Res. A* **571** 263–6
- Humm J L, Rosenfeld A and Del Guerra A 2003 From PET detectors to PET scanners *Eur. J. Nucl. Med. Mol. Imaging* **30** 1574–97
- Jan S et al 2004 GATE: a simulation toolkit for PET and SPECT *Phys. Med. Biol.* **49** 4543–61
- Jan S et al 2011 GATE v6: a major enhancement of the GATE simulation platform enabling modelling of CT and radiotherapy *Phys. Med. Biol.* **56** 881–901
- Karlberg A M et al 2016 Quantitative comparison of PET performance—Siemens biograph mCT and mMR *Eur. J. Nucl. Med. Mol. Imaging Phys.* **3** 5
- Karp J S et al 2008 Benefit of time-of-flight in PET: experimental and clinical results *J. Nucl. Med.* **49** 462–70
- Korcyl G et al 2016 Sampling FEE and trigger-less DAQ for the J-PET scanner *Acta Phys. Pol. B* **47** 492–6
- Korcyl G et al 2018 Evaluation of single-chip, real-time tomographic data processing on FPGA—SoC devices *IEEE Trans. Med. Imaging* in print <https://doi.org/10.1109/tmi.2018.2837741>
- Kowalski P et al 2015 Multiple scattering and accidental coincidences in the J-PET detector simulated using GATE package *Acta Phys. Pol. A* **127** 1505–12
- Kowalski P et al 2016 Scatter fraction of the J-PET tomography scanner *Acta Phys. Pol. B* **47** 549–60
- Krzemień W et al 2015 Analysis framework for the J-PET scanner *Acta Phys. Pol. A* **127** 1491–4
- Lacy J et al 2010 New PET scanner for small animal imaging based on innovative straw detector technology *J. Nucl. Med.* **51** 190
- Moses W W 2003 Time of flight in PET revisited *IEEE Trans. Nucl. Sci.* **50** 1325–30
- Moses W W and Derenzo S E 1999 Prospects for time-of-flight PET using LSO scintillator *IEEE Trans. Nucl. Sci.* **46** 474–8
- Moskal P 2018 Total body PET—from mice to men (Ghent 2018)
- Moskal P et al 2011 Novel detector systems for the positron emission tomography *Bio-Algorithms Med-Syst.* **7** 73–8
- Moskal P et al 2014 Test of a single module of the J-PET scanner based on plastic scintillators *Nucl. Instrum. Methods Phys. Res. A* **764** 317–21
- Moskal P et al 2015 A novel method for the line-of-response and time-of-flight reconstruction in TOF-PET detectors based on a library of synchronized model signals *Nucl. Instrum. Methods Phys. Res. A* **775** 54–62
- Moskal P et al 2016 Time resolution of the plastic scintillator strips with matrix photomultiplier readout for J-PET tomograph *Phys. Med. Biol.* **61** 2025–47
- NEMA 2012 Performance measurements of positron emission tomographs NEMA standards publication (NEMA NU 2-2012)
- Niedźwiecki S Z et al 2017 J-PET: a new technology for the whole-body PET imaging *Acta Phys. Pol. B* **48** 1567
- Oliver J F and Rafecas M 2016 Modelling random coincidences in positron emission tomography by using singles and prompts: a comparison study *PLoS ONE* **11** e0162096
- Pałka M et al 2017 Multichannel FPGA based MVT system for high precision time (20 ps RMS) and charge measurement *J. Instrum.* **12** P08001
- Philips 2018a Philips vereos PET/CT brochure http://incenter.medical.philips.com/doclib/enc/10264938/452296298357_VereosBrochureREV_FNL_HR.pdf (Accessed: 29 March 2018)
- Philips 2018b www.philips.ca/healthcare/product/HC882471/gemini-tf-pet-ct-scanner (Accessed: 29 March 2018)
- Raczyński L et al 2014 Novel method for hit-position reconstruction using voltage signals in plastic scintillators and its application to positron emission tomography *Nucl. Instrum. Methods Phys. Res. A* **764** 186–92
- Raczyński L et al 2015 Compressive sensing of signals generated in plastic scintillators in a novel J-PET instrument *Nucl. Instrum. Methods Phys. Res. A* **786** 105–12
- Reynés-Llompart G et al 2017 Performance characteristics of the whole-body discovery IQ PET/CT system *J. Nucl. Med.* **58** 1155–61
- Shopa R Y et al 2017 Three-dimensional image reconstruction in J-PET using filtered back projection method *Acta Phys. Pol. B* **48** 1757
- Siemens 2018 www.activexray.com/pdf/Siemens_Biograph.pdf (Accessed: 29 March 2018)
- Slomka P et al 2016 Recent advances and future progress in PET instrumentation *Semin. Nucl. Med.* **46** 5–19
- Smyrski J et al 2017 Measurement of gamma quantum interaction point in plastic scintillator with WLS strips *Nucl. Instrum. Methods Phys. Res. A* **851** 39–42
- Solevi P et al 2015 AX-PET: from demonstrator towards a full-ring brain scanner *Acta Phys. Pol. A* **127** 1462–4
- Surti S et al 2007 Performance of philips Gemini TF PET/CT scanner with special consideration for its time-of-flight imaging capabilities *J. Nucl. Med.* **48** 471–80
- Teras M et al 2007 Performance of the new generation of whole-body PET/CT scanners: Discovery STE and Discovery VCT *Eur. J. Nucl. Med. Mol. Imaging* **34** 1683–92
- Thielemans K et al 2012 STIR: software for tomographic image reconstruction release 2 *Phys. Med. Biol.* **57** 867
- Townsend D W 2004 Physical principles and technology of clinical PET imaging *Ann. Acad. Med. Singap.* **33** 133–45

Vandenberghe S *et al* 2016 Recent developments in time-of-flight PET *Eur. J. Nucl. Med. Mol. Imaging Phys.* **3** 3

Viswanath V *et al* 2017 Development of PET for total-body imaging *Acta Phys. Pol. B* **48** 1555–66

Yang X and Peng H 2015 The use of noise equivalent count rate and the NEMA phantom for PET image quality evaluation *Phys. Med.* **31** 179–84

Zhang X *et al* 2017 Quantitative image reconstruction for total-body PET imaging using the 2-meter long EXPLORER scanner *Phys. Med. Biol.* **62** 2465